



Article

Janus Type Monolayers of S-MoSiN₂ Family and Van Der Waals Heterostructures with Graphene: DFT-Based Study

Ruslan M. Meftakhutdinov¹ and Renat T. Sibatov^{1,2,*}

¹ Laboratory of Diffusion Processes, Ulyanovsk State University, 432017 Ulyanovsk, Russia; postbox.mrm@gmail.com

² Scientific-Manufacturing Complex "Technological Centre", 124498 Moscow, Russia

* Correspondence: ren_sib@bk.ru

Abstract: Novel representative 2D materials of the Janus type family X-M-ZN₂ are studied. These materials are hybrids of a transition metal dichalcogenide and a material from the MoSi₂N₄ family, and they were constructed and optimized from the MoSi₂N₄ monolayer by the substitution of SiN₂ group on one side by chalcogen atoms (sulfur, selenium, or tellurium), and possibly replacing molybdenum (Mo) to tungsten (W) and/or silicon (Si) to germanium (Ge). The stability of novel materials is evaluated by calculating phonon spectra and binding energies. Mechanical, electronic, and optical characteristics are calculated by methods based on the density functional theory. All considered 2D materials are semiconductors with a substantial bandgap (>1 eV). The mirror symmetry breaking is the cause of a significant built-in electric field and intrinsic dipole moment. The spin-orbit coupling (SOC) is estimated by calculations of SOC polarized bandstructures for four most stable X-M-ZN₂ structures. The possible van der Waals heterostructures of considered Janus type monolayers with graphene are constructed and optimized. It is demonstrated that monolayers can serve as outer plates in conducting layers (with graphene) for shielding a constant external electric field.



Citation: Meftakhutdinov, R.M.; Sibatov, R.T. Janus Type Monolayers of S-MoSiN₂ Family and Van Der Waals Heterostructures with Graphene: DFT-Based Study. *Nanomaterials* **2022**, *12*, 3904. <https://doi.org/10.3390/nano12213904>

Academic Editor: Andres Castellanos-Gomez

Received: 29 September 2022

Accepted: 31 October 2022

Published: 5 November 2022

Publisher's Note: MDPI stays neutral with regard to jurisdictional claims in published maps and institutional affiliations.



Copyright: © 2022 by the authors. Licensee MDPI, Basel, Switzerland. This article is an open access article distributed under the terms and conditions of the Creative Commons Attribution (CC BY) license (<https://creativecommons.org/licenses/by/4.0/>).

Keywords: Janus 2D material; transition metal dichalcogenide; van der Waals heterostructure

1. Introduction

Recently [1], centimeter-scale monolayer films of 2D material MoSi₂N₄ were obtained by introducing elemental silicon during growth of non-layered molybdenum nitride by chemical vapor deposition. Successful formation of analogous 2D material WSi₂N₄ with a similar approach was evidence of the concept versatility. The method opened up opportunities for elaboration of a family of stable 2D materials for which there are no natural layered 3D crystals [2].

Two-dimensional MoSi₂N₄ consists of a MoN₂ monolayer sandwiched between two Si-N layers. MoSi₂N₄ demonstrates semiconducting behavior with excellent ambient air stability. MoSi₂N₄ is characterized by an elastic constant three times higher than a constant of 2D transition metal dichalcogenide MoS₂. The electron and hole mobilities in MoSi₂N₄ are approximately 4 and 6 times higher than for MoS₂. High carrier mobility coupled with high environmental stability makes this material promising for use in various nanoelectronic applications.

A large number of similar 2D materials with general formula MA₂Z₄ (M = Mo, W, V, Nb, Ta, Ti, Zr, Hf or Cr; A = Si or Ge, Z = N, P or As) were predicted by means of the density functional theory (DFT) based computations and investigated using computational methods (see, e.g., [3,4]). The predicted monolayers are characterized by a wide range of properties from semiconductor to metallic; some compounds with magnetic transition metal elements also have magnetic properties [5]. MoSi₂N₄ and WSi₂N₄ monolayers also exhibit high lattice thermal conductivity for thermoelectric applications [6]. Most of the 2D materials from the discussed family also have a suitable band gap of up to 1.7 eV for potential optical applications in the visible range [7,8].

In our recent work [9], for the first time, we proposed and theoretically investigated the asymmetric 2D materials XMoSiN_2 ($X = \text{S, Se, Te}$), constructed and optimized from MoSi_2N_4 by substitution of SiN_2 group on one side of MoSi_2N_4 by chalcogen atoms (sulfur, selenium, or tellurium). The constructed 2D materials are hybrids of a transition metal dichalcogenide and a 2D material from the MoSi_2N_4 family. They can be considered as a Janus type 2D material with mirror symmetry breaking. Hypothetically, the experimental methods of chalcogen replacement in conventional 2D transition-metal dichalcogenides to form Janus-type heterostructures (see, e.g., [10–12]) can be conformed to obtain the proposed layers.

The geometry of the structures under consideration is presented in Figure 1. Parameters of novel optimized structures are provided in Section 2. The stability is substantiated by DFT-based calculations of phonon bandstructures and binding energies. The mirror symmetry breaking and significant difference in electronegativity of chalcogen atoms and an SiN_2 group lead to high intrinsic electric field. A large built-in transverse electric field enables separation of the generated electron–hole pairs within a monolayer that is promising particularly for photovoltaic applications.

Recently, Rezavand and Ghobadi [13] studied the structural, electronic, and spintronic features of similar Janus MTeSiX_2 ($M = \text{Mo, W}$; $X = \text{N, P, As}$) monolayers by computational methods. Calculated phonon bandstructures and cohesive energies indicate the stability of these Janus monolayers. The considered Janus type monolayers demonstrate a semiconducting behavior with a sufficient bandgap. The authors confirmed a high intrinsic electric field caused by breaking out-of-plane symmetry. This field induces Rashba spin–orbit coupling. In addition, the authors observed non-parabolic Mexican hat-like dispersion at the Γ -point of the valence band. Studies [9,13] enriched a Janus 2D materials family by novel candidates for next-generation spintronic or photovoltaic devices.

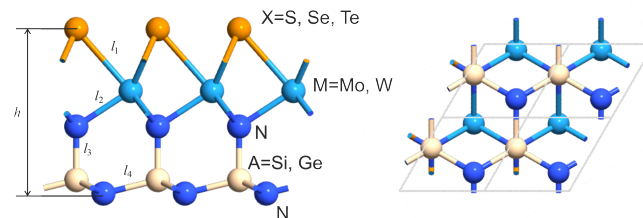


Figure 1. Geometry of the XMAN_2 monolayer. Lattice parameter, bond lengths, and thickness are listed in Table 1.

Table 1. Lattice parameter a , bond lengths l_1, l_2, l_3, l_4 and thickness h of optimized Janus structures X-M-AN_2 ($X = \text{S, Se, Te}$; $M = \text{Mo, W}$, $A = \text{Si, Ge}$) and formation energy E_{form} .

	$a, \text{Å}$	$l_1, \text{Å}$	$l_2, \text{Å}$	$l_3, \text{Å}$	$l_4, \text{Å}$	$h, \text{Å}$	$E_{\text{form}}, \text{eV/atom}$
SWSiN_2	2.999	2.39	2.12	1.77	1.80	5.13	−0.93
SeWSiN_2	3.042	2.55	2.13	1.77	1.82	5.29	−0.70
TeWSiN_2	3.113	2.72	2.15	1.77	1.85	5.44	−0.37
SWGGeN_2	3.105	2.47	2.14	1.77	1.85	5.08	−0.38
SeWGeN_2	3.132	2.56	2.15	1.91	1.90	5.47	−0.26
TeWGeN_2	3.105	2.72	2.14	1.77	1.85	5.43	−0.12
SMoGeN_2	3.127	2.27	2.14	1.77	1.86	4.67	−0.21
SeMoGeN_2	3.125	2.54	2.14	1.90	1.90	5.44	−0.33
TeMoGeN_2	3.193	2.72	2.16	1.91	1.93	5.60	−0.06
SMoSiN_2 [9]	2.989	2.38	2.11	1.76	1.80	5.12	−0.96
SeMoSiN_2 [9]	3.034	2.53	2.12	1.77	1.83	5.27	−0.77
TeMoSiN_2 [9]	3.105	2.72	2.14	1.77	1.85	5.43	−0.46

In this paper, we supplement the family of asymmetric structures X-M-ZN₂ by novel representative 2D materials (namely, X = S, Se, Te; M = Mo, W; A = Si, Ge). In addition, we consider van der Waals heterostructures (vdW) of Janus type S-Mo-SiN₂ with graphene and estimate their basic properties.

2. Optimization and Stability of Structures

Presented computational results were obtained within the density functional theory (DFT) implemented in the Quantum ATK package [14]. To optimize the initial structures and to relax materials under stress, we have chosen pseudopotential PseudoDojo [15] with a linear combination of atomic orbitals (LCAO). The exchange–correlation potential was described by the generalized Perdew–Burke–Ernzerhof gradient approximation (GGA-PBE) [16]. The 15 × 15 × 1 grid in the first Brillouin zone was used for optimization.

The structures were optimized until the maximum force acting on each atom becomes less than 0.01 eV/Å, and the maximum energy change between two stages becomes less than 10^{−5} eV. To avoid the influence of boundary conditions in the direction perpendicular to the 2D sheet, the lattice cell parameter 30 Å is used. The band structures, optical properties, and spin-polarized characteristics were calculated using the Heyd–Scuseria–Ernzerhof (HSE06) hybrid exchange–correlation functional. The 25 × 25 × 1 grid in the first Brillouin zone was used to calculate the electronic and optical properties.

The formation energy per atom is calculated according to the following formula:

$$E_{\text{form}} = \frac{E_{\text{total}} - E(\text{M} = \text{Mo}, \text{W}) - E(\text{A} = \text{Si}, \text{Ge}) - E(\text{X} = \text{S}, \text{Se}, \text{Te}) - 2E(\text{N})}{N},$$

where E_{total} is the total energy of cluster, E are energies of elements calculated for optimized Mo, W, α – Si, α – Ge, orthorhombic sulfur, γ – Se, α – Te, and molecules N₂; N is the number of atoms in the translated cluster (unit cell).

Figure 1 shows the structure of studied X-M-AN₂ layers and indicates the main geometric parameters. Calculated values of these parameters are listed in Table 1. The results of calculation for the negative formation energy are also given there.

All proposed structures have a negative formation energy, which means that they should be stable. Furthermore, we limit our consideration on the following most stable structures: SWSiN₂, SeWSiN₂, TeWSiN₂, and SWGeN₂.

In equilibrium, the potential energy is minimal, and it increases with small displacements of atoms from the positions of stable configuration. This fact makes it possible to use vibrational spectra as a criterion for the stability of materials [17]. To estimate the dynamic stability of optimized structures, the phonon dispersion characteristics of monolayers were calculated (Figure 2). The elementary cell contains five atoms, so its phonon spectrum consists of 15 phonon branches, 3 acoustic and 12 optical. Three acoustic branches have a lower frequency and contain in-plane longitudinal (LA), transverse (TA) and out-of-plane (ZA) acoustic modes. There are no imaginary frequencies in the Brillouin zone, except for small fragments near the Γ point formed by the ZA mode. The maximum values of these frequencies are 0.165, 0.285, 0.141, and 0.771 meV (or 1.33, 2.30, 1.41, and 6.22 cm^{−1}) for SeWSiN₂, TeWSiN₂, SWSiN₂, and SWGeN₂, respectively. This slight instability is due to the difficulty of achieving numerical convergence for the flexural acoustic phonons (ZA) branch when using first principles calculations for 2D materials. In addition, even higher imaginary frequencies of 14 and 280 cm^{−1} were reported for 1T'-MY₂ monolayers (M = Mo, W; Y = S, Se, Te) [18] and 1T-MoS₂ [19], respectively.

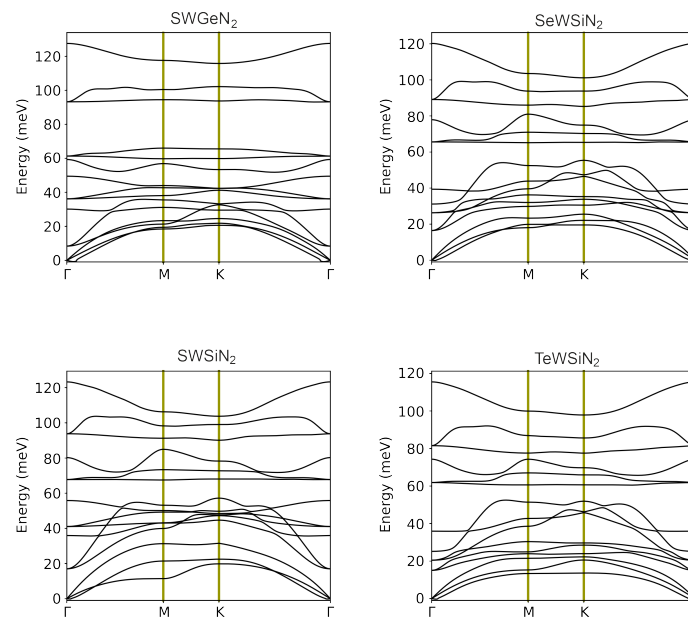


Figure 2. Phonon spectra of X-M-AN₂ monolayers. The three lower branches correspond to acoustic modes TA, LA, and ZA, and the remaining 12 branches represent optical modes. The intersection of the optical branches at the Γ point indicates their degeneracy.

Twelve optical modes comprise 4 in-plane longitudinal (LO), 4 in-plane transverse (TO), and 4 out-of-plane (ZO) optical modes. Based on irreducible representations at point Γ , these modes are classified as doubly degenerate E (LO and TO) non-degenerate A_1 (ZO). There is no frequency gap between the acoustic and optical branches, and the conservation law for energy in phonon–phonon scattering is easy to fulfill, which leads to a high phonon scattering rate. In particular, the process of annihilation of two acoustic modes into one optical mode becomes highly efficient.

3. Electronic Properties of Structures

Figure 3 demonstrates band structures obtained using PBE and HSE06 exchange–correlation functionals. The calculation results with HSE06 show that SWSiN₂ is a direct-gap semiconductor with the conduction band minimum (CBM) and valence band maximum (VBM) located at the same point K. Applying PBE to this structure makes it indirect-gap and changes the transition to $\Gamma \rightarrow K$. The CBM and VBM of the remaining monolayers lie at different points, giving rise to indirect band structures for both functionals. Table 2 lists the bandgap values for considered monolayers. The value of E_g^{PBE} is expectedly less than E_g^{HSE06} . In further calculations, the HSE06 functional is used because for bandgaps, and it gives smaller errors than PBE [20].

Absorption spectra of XMAN₂ monolayers are presented in Figure 4. The used computational approach is based on the Kubo–Greenwood formalism and described particularly in [9,21].

In the structures under study, spin–orbit splitting (SOC) can be observed due to the absence of a horizontal reflection plane. In Figure 5, the projected bandstructures calculated taking into account the SOC interaction are presented. It can be seen that the interaction reduces the bandgap. In addition, for SeWSiN₂, SOC shifts VBM from the valley $K \rightarrow \Gamma$ to point K, and SWSiN₂ becomes an indirect-gap semiconductor.

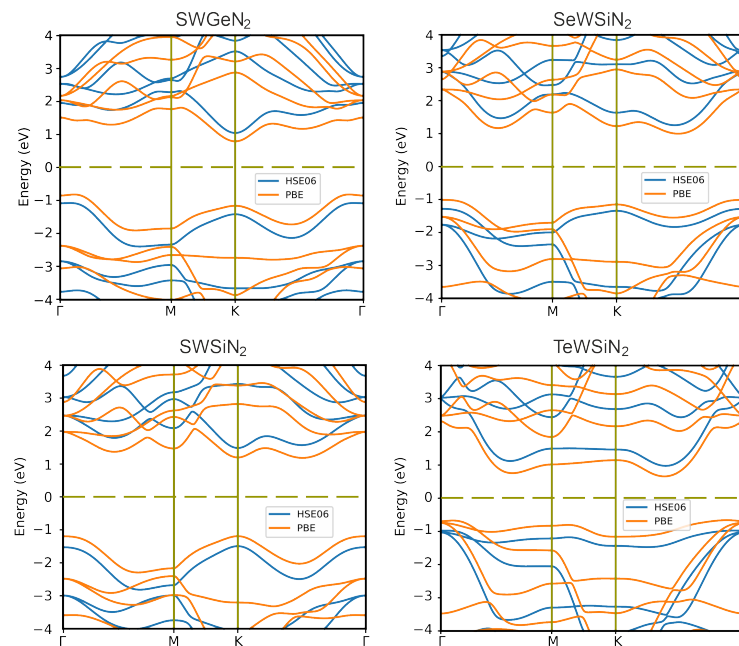


Figure 3. Band structures of 2D XMoSiN₂ (X = S, Se, Te) calculated using PBE (orange lines) and HSE06 (blue lines) functionals. The dashed line represents the Fermi level.

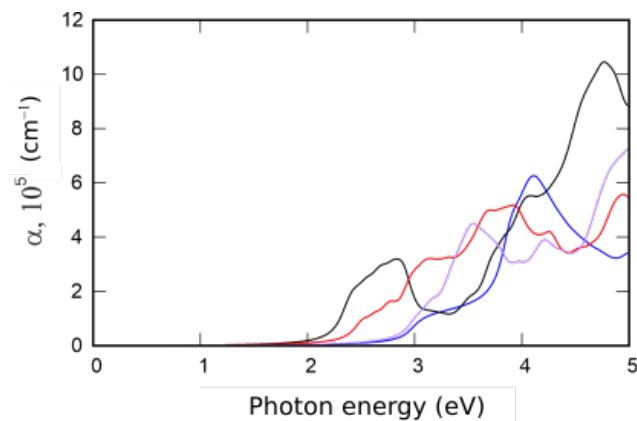


Figure 4. Absorption coefficient of XMAN₂: SWSiN₂ (blue line), TeWSiN₂ (black line), SWGeN₂ (red line), and SeWSiN₂ (purple line).

In Figure 5, one can find that the electronic states near CBM and VBM are mainly associated with the *d*-orbitals of the tungsten atom, and only VBM of SWGeN₂ and TeWSiN₂ are also partially represented by N-*p_z* states.

Strong hybridization between the *W-d_{x²-y²}* and *W-d_{xy}* orbitals results in a large SOC splitting. For all structures, the maximum splitting of the valence band is found at the K point, while for the conduction band in the K → Γ and Γ → M valleys splitting values of the valence and conduction bands.

In Figures 6 and 7, we additionally investigate vertical polarization by plotting the electrostatic potential and electron density difference along the *z*-axis. All structures have an electrostatic potential difference $\Delta\phi$, with the potential being higher on the side of the external nitrogen atom. In addition, there is a redistribution of electrons. The central nitrogen atom, due to its high electronegativity (3.04), pulls electrons from neighboring tungsten, silicon, or germanium atoms for SWGeN₂ (the electronegativity values are 2.36, 1.9, and 2.01, respectively). Moreover, from the side of W, Δn_e is larger than from the side of Si or Ge because tungsten has more electrons. The outer nitrogen atom also pulls electrons from silicon, but to a lesser extent than the central one. The electronegativity of the external chalcogens Se and S (2.55 and 2.58, respectively) is slightly higher than the electronegativity of W, so the

maximum electron concentration is at the interface between tungsten and selenium or sulfur and is slightly shifted to the latter, in contrast to Te (2.10), where the electrons are concentrated, on the contrary, closer to the metal. Charge depletion is observed on the chalcogen atoms themselves. Due to the redistribution of electrons, local electric fields arise, one directed from the outer nitrogen atom to the central one, and the other from the chalcogenide atom to the central N. Thus, a resulting field arises directed from the chalcogen atom to the outer nitrogen. The largest intensity of this built-in field is in SeWSiN₂ 1.91 VÅ⁻¹, for TeWSiN₂ it is 1.86 VÅ⁻¹, for SWSiN₂–1.31 VÅ⁻¹, and for SWGeN₂–0.90 VÅ⁻¹. This indicates a stronger vertical polarization of the SeWSiN₂ monolayer. A positive charge at the boundary of the structure (Se, S, and Te atoms) facilitates the escape of electrons, which leads to a decrease in the work function and the potential energy difference of 2.01 eV, 1.61 eV, and 0.47 eV for TeMoSiN₂, SeMoSiN₂, and SMOsiN₂, respectively.

The built-in field promotes charge separation, which makes these structures promising for photocatalysis and optoelectronics. The positive charge at the boundary (Se, S, and Te atoms) facilitates the escape of electrons that leads to a decrease in the work function and the potential energy difference. In addition, a dipole moment μ proportional to $\Delta\phi$ arises. Due to the large electronegativity difference between Te and nitrogen, TeWSiN₂ has the largest dipole moment (Table 2).

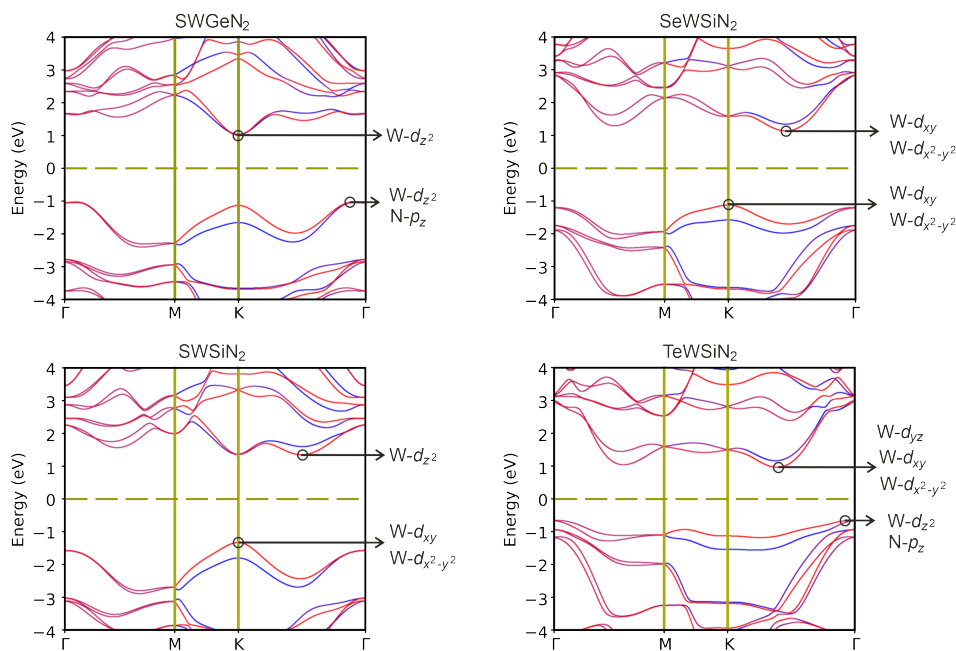


Figure 5. Band structures XMOSiN₂ (X = S, Se, Te) calculated using HSE06+SOC. Inserts indicate the states forming VBM and CBM.

Table 2. Bandgap E_g calculated using PBE, HSE06, and HSE06+SOC functionals, SOC splitting Δ_V for valence band maximum and Δ_C for conduction band minimum, potential energy difference $\delta\phi$ and dipole moment μ in Janus structures X-W-AN₂ (X = S, Se, Te; A = Si, Ge).

	E_g^{PBE} , eV	E_g^{HSE06} , eV	$E_g^{\text{HSE06+SOC}}$, eV	Δ_V , meV	Δ_C , meV	$\Delta\phi$, eV	μ , D
SWSiN ₂	2.37	2.98	2.67	475	254	0.65	0.238
SeWSiN ₂	2.01	2.54	2.26	329	454	1.60	0.403
TeWSiN ₂	1.32	1.95	1.62	410	406	2.05	0.530
SWGeN ₂	1.61	2.12	2.03	523	219	0.42	0.224

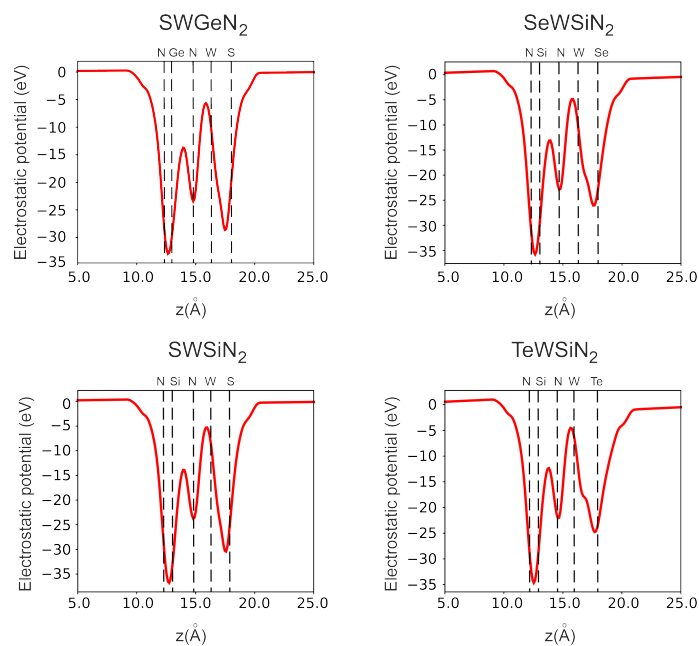


Figure 6. Electrostatic potential in X-W-AN₂ (X = S, Se, Te, A = Si, Ge). Dashed lines indicate the positions of atoms.

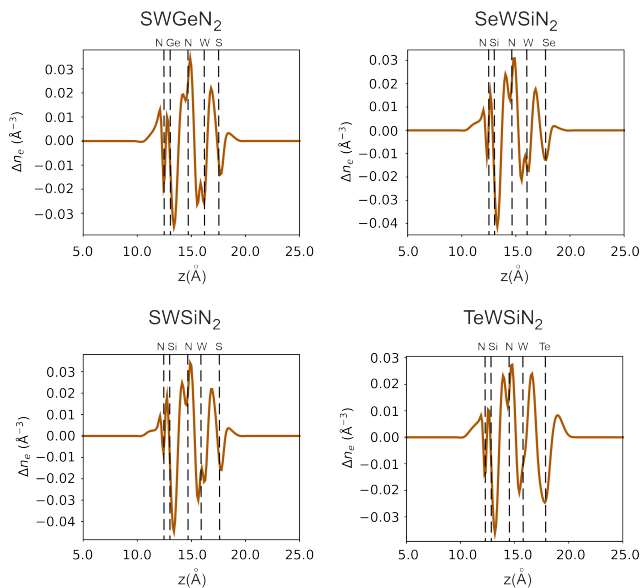


Figure 7. Monolayer electron difference density in X-W-AN₂ (X = S, Se, Te, A = Si, Ge).

One way to change the bandgap is to stretch the monolayer in the plane. Figure 8 shows the stress (a) and bandgap (b) versus strain. In addition, elastic moduli, Young’s modulus Y , and Poisson’s ratio ν are listed in Table 3. Deviation from the linear Hooke’s law takes place at deformations greater than 0.1% for SWGeN_2 and SeWSiN_2 , for SWSiN_2 and TeWSiN_2 deviation from linearity is observed at deformations exceeding 3% (Figure 8a). Due to the higher Young’s modulus, SeWSiN_2 stretches worse than other structures, and when it reaches 10% deformation, it fractures. For comparison, the values of elastic moduli for graphene and MoS_2 are also given. Young’s modulus of XWSiN_2 is close to the value of graphene and is 2.5 times higher than that of two-dimensional molybdenite. Poisson’s ratio of SWGeN_2 is close to values of TMDs.

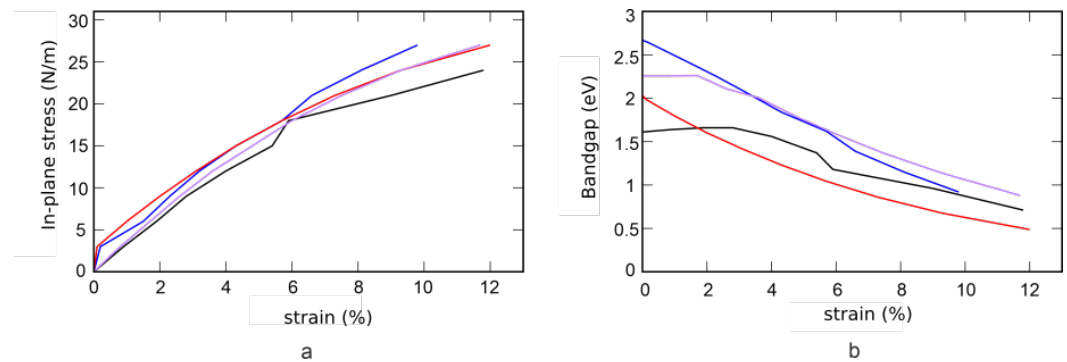


Figure 8. Dependences of stress (a) and band gap (b) on strain. SWSiN₂ (blue line), TeWSiN₂ (black line), SWGeN₂ (red line), and SeWSiN₂ (purple line).

Deformation of the structure in the plane changes the bandgap. The gap of SWSiN₂ and TeWSiN₂ changes irregularly with deformation: at first, it slightly increases and then decreases. SWGeN₂ and SeWSiN₂ behave more predictably. The linear decrease in the SeWSiN₂ gap to a strain of 6% makes this material promising for use in flexible electronics.

Table 3. Elasticity moduli, Young's modulus Y , Poisson's ratio ν for Janus monolayers X-W-AN₂ (X = S, Se, Te, A = Si, Ge), compared with those for graphene and MoS₂.

	c_{11} , N/m	c_{12} , N/m	c_{66} , N/m	Y , N/m	ν
SWSiN ₂	339.43	74.59	131.88	323.04	0.22
SeWSiN ₂	339.47	69.79	130.83	325.12	0.21
TeWSiN ₂	312.24	56.95	130.34	301.85	0.18
SWGeN ₂	274.17	68.64	100.68	256.99	0.25
MoS ₂	128.40	32.60	–	120.10	0.25
graphene	352.00	62.60	–	340.80	0.18

4. Van Der Waals Heterostructures with Graphene

Van der Waals heterostructures based on 2D layered materials with selected properties pave the way for integration at the atomic level and can lead to new heterostructures with completely new physics and versatility. Janus 2D materials with different surfaces have attracted intensive research interest due to the remarkable properties induced by symmetry breaking. In recent times, various vdW heterostructures with Janus TMDCs have been studied [22–24]. In our recent works [25,26], we proposed and studied novel vdW heterostructures obtained by stacking of graphenylene with TMDCs and Janus XMoY (X \neq Y = S, Se, Te) monolayers.

In [27], the authors studied vdW heterostructures consisting of MoSi₂N₄ in contact with graphene and NbS₂ monolayers using the density functional theory calculations. They have shown that the MoSi₂N₄/NbS₂ contact exhibits an ultra-low Schottky barrier height, which is beneficial for nanoelectronics' applications. For the MoSi₂N₄/graphene contact, the Schottky barrier height can be modulated with interlayer spacing or with external electric fields. The maximum of absorption spectrum falls at a wavelength of 510 nm. The tube is characterized by significant optical absorption in the entire optical range.

Apparently, it is possible to form a van der Waals contact of the Janus layers considered here with graphene and two-dimensional dichalcogenides. We consider structures with graphene in more detail (Figure 9). Table 4 provides information about geometric parameters of optimized vdW heterostructures graphene/S-MoSiN₂ and S-MoSiN₂/graphene. The optimization was performed with exchange–correlation potential described by PBE GGA [16], with vdW corrections incorporated with Grimme's DFT-D2 method [28]. The structure optimization is carried out until the maximum force on each atom becomes less than 0.01 eV/Å, and the maximum energy change between the two steps is smaller than 10^{−5} eV. In both structures, the graphene was stretched ($\epsilon \approx 2.8\%$), while the Janus

monolayer S-MoSiN₂ was compressed ($\epsilon \approx -1.9\%$) after optimization of vdW junction. Electrostatic potential and electron difference density for these vdW heterostructures are plotted in Figure 10.

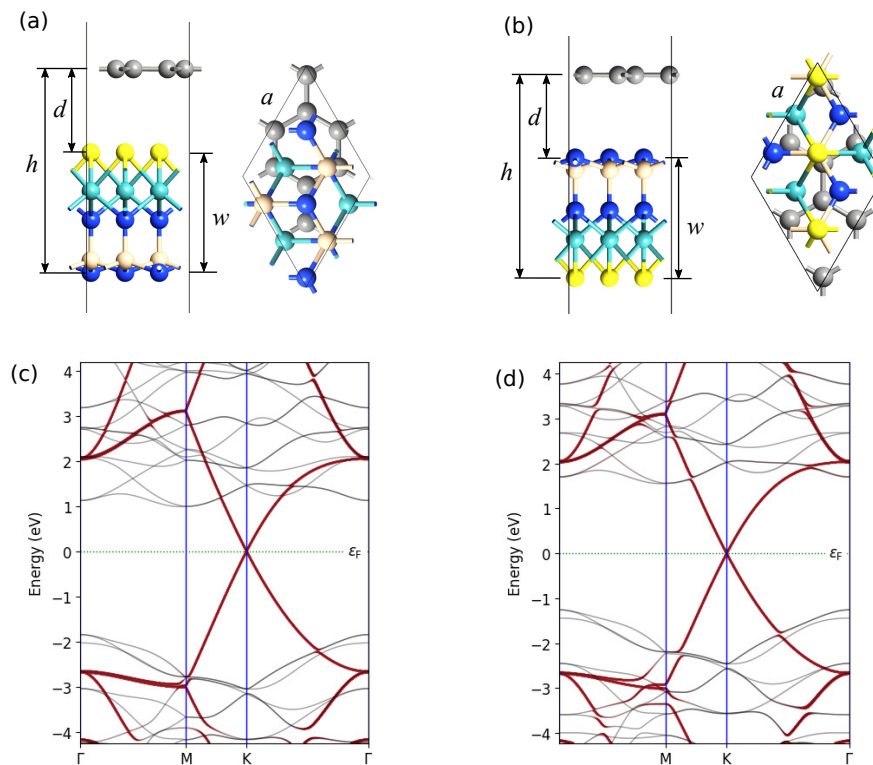


Figure 9. Geometry of vdW heterostructure S-MoSiN₂/graphene and graphene/S-MoSiN₂ (a,b) and their bandstructures (c,d). The brown lines correspond to the contribution of carbon.

A large built-in transverse electric field in Janus X-M-ZN₂ monolayers can be utilized in photovoltaic applications. Also, we show that these monolayers can serve as shielding layers. In Figure 11, geometry of three-layer vdW junction S-MoSiN₂/graphene/S-MoSiN₂ is shown. Calculated bandstructures corresponding to three values of electric field: 0 V/nm, 0.667 V/nm, and 1.333 V/nm indicate that the branches corresponding to the graphene contribution are insensitive to an external transverse electric field in such a structure. In this case, the branches corresponding to the Janus layers shift significantly.

Table 4. Geometric parameters of vdW heterostructures graphene/S-MoSiN₂ and S-MoSiN₂/graphene.

	$h, \text{\AA}$	$d, \text{\AA}$	$w, \text{\AA}$	$a, \text{\AA}$
graphene/S-MoSiN ₂	8.771	3.597	5.1739	5.080
S-MoSiN ₂ /graphene	8.736	3.564	5.1725	5.081

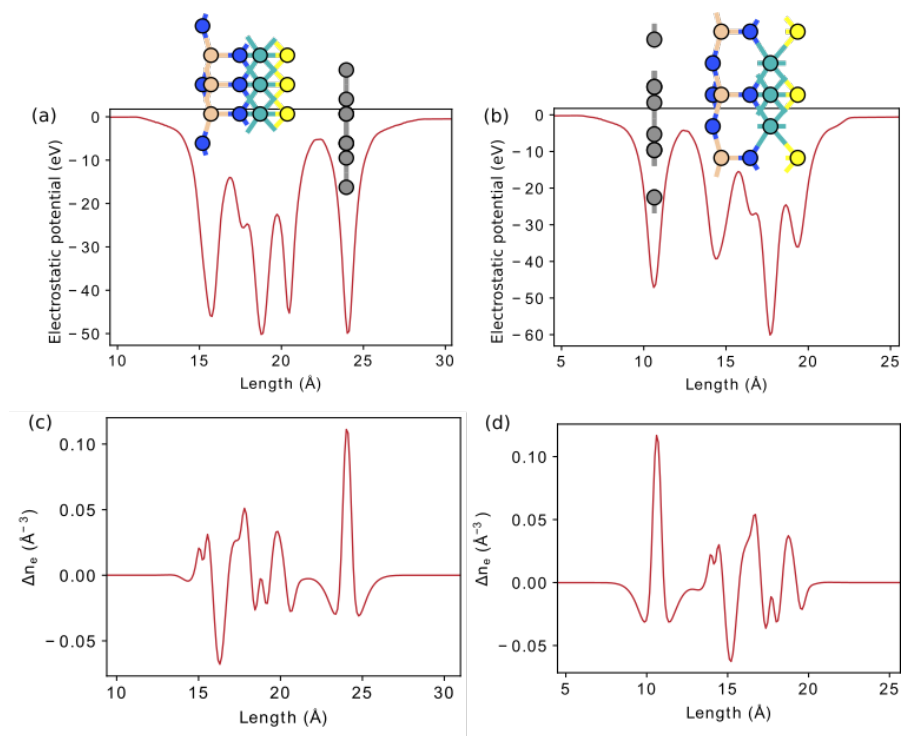


Figure 10. Electrostatic potential and electron difference density for vdW heterostructure S-MoSiN₂/graphene (a,c) and graphene/S-MoSiN₂ (b,d).

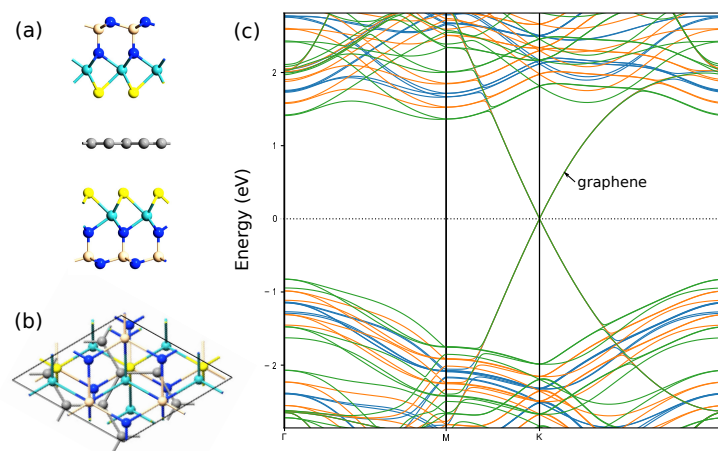


Figure 11. Geometry of three-layer vdW heterostructure S-MoSiN₂/graphene/S-MoSiN₂ (a,b). Bandstructures (c) are calculated for three values of electric field: 0 V/nm (blue line), 0.667 V/nm (orange line), and 1.333 V/nm (green line).

5. Conclusions

In our recent work [9], for the first time, we proposed and theoretically investigated the asymmetric 2D materials XMoSiN₂ (X = S, Se, Te), constructed and optimized from MoSi₂N₄. In this work, we continue studying other representatives of the Janus type monolayers X-M-ZN₂ (X = S, Se, Te; M = Mo, W; A = Si, Ge). These monolayers were constructed and optimized from MoSi₂N₄ by replacing SiN₂ on one side with chalcogen atoms (sulfur, selenium, or tellurium), and possibly replacing molybdenum (Mo) to tungsten (W) and/or silicon (Si) to germanium (Ge). The new structure is a hybrid of a transition metal dichalcogenide and a 2D material from the MoSi₂N₄ family. The stability of new 2D materials has been substantiated by means of DFT-based calculations. The monolayers under study are characterized by high values of binding energy >7.5 eV/atom. First-principle studies of

several representatives, such as MTeSiX_2 ($\text{M} = \text{Mo}, \text{W}; \text{X} = \text{N}, \text{P}, \text{As}$) monolayers, were studied in [13]. In all studied monolayers, a large built-in transverse electric field arises due to the redistribution of electrons, enabling separation of the generated electron-hole pairs within one layer that is promising for photovoltaic applications. Possible vdW heterostructures of Janus type monolayers with graphene are estimated. It is particularly shown that the Janus type MoSSiN_2 monolayers effectively shield a constant external electric field.

Author Contributions: Investigation, R.M.M. and R.T.S.; methodology, R.M.M. and R.T.S.; software, R.T.S.; writing—original draft, R.M.M.; writing—review & editing, R.T.S. All authors have read and agreed to the published version of the manuscript.

Funding: This work was supported by the Ministry of Science and Higher Education of the Russian Federation (project # 075-15-2021-581).

Data Availability Statement: Not applicable.

Conflicts of Interest: The authors declare no conflict of interest.

References

- Hong, Y.-L.; Liu, Z.; Wang, L.; Zhou, T.; Ma, W.; Xu, C.; Feng, S.; Chen, L.; Chen, M.-L.; Sun, D.-M.; et al. Chemical vapor deposition of layered two-dimensional MoSi_2N_4 materials. *Science* **2020**, *369*, 670–674. [[CrossRef](#)] [[PubMed](#)]
- Novoselov, K.S. Discovery of 2d van der Waals layered MoSi_2N_4 family. *Natl. Sci. Rev.* **2020**, *7*, 1842–1844. [[CrossRef](#)] [[PubMed](#)]
- Wang, L.; Shi, Y.; Liu, M.; Zhang, A.; Hong, Y.-L.; Li, R.; Qiang, G.; Chen, M.; Ren, W.; Cheng, H.-M.; et al. Intercalated architecture of MA_2Z_4 family layered van der waals materials with emerging topological, magnetic and superconducting properties. *Nat. Commun.* **2021**, *12*, 1–10.
- Zhong, H.; Xiong, W.; Lv, P.; Yu, J.; Yuan, S. Strain-induced semiconductor to metal transition in MA_2Z_4 bilayers ($\text{M} = \text{Ti}, \text{Cr}, \text{Mo}; \text{A} = \text{Si}; \text{Z} = \text{N}, \text{P}$). *Phys. Rev. B* **2021**, *103*, 085124. [[CrossRef](#)]
- Akanda, M.; Karim, R.; Lake, R.K. Magnetic properties of NbSi_2N_4 , VSi_2N_4 , and VSi_2P_4 monolayers. *arXiv* **2021**, arXiv:2105.01857.
- Li, B.; Geng, J.; Ai, H.; Kong, Y.; Bai, H.; Lo, K.H.; Ng, K.W.; Kawazoe, Y.; Pan, H. Design of 2d materials— $\text{MSi}_2\text{C}_x\text{N}_4\text{-X}$ ($\text{M} = \text{Cr}, \text{Mo}$, and $\text{W}; x = 1$ and 2)—with tunable electronic and magnetic properties. *Nanoscale* **2021**, *13*, 8038–8048. [[CrossRef](#)]
- Mortazavi, B.; Javvaji, B.; Shojaei, F.; Rabczuk, T.; Shapeev, A.V.; Zhuang, X. Exceptional piezoelectricity, high thermal conductivity and stiffness and promising photocatalysis in two-dimensional MoSi_2N_4 family confirmed by first-principles. *Nano Energy* **2021**, *82*, 105716. [[CrossRef](#)]
- Yu, J.; Zhou, J.; Wan, X.; Li, Q. High intrinsic lattice thermal conductivity in monolayer MoSi_2N_4 . *New J. Phys.* **2021**, *23*, 033005. [[CrossRef](#)]
- Sibatov, R.T.; Meftakhutdinov, R.M.; Kochaev, A.I. Asymmetric XMoSiN_2 ($\text{X} = \text{S}, \text{Se}, \text{Te}$) monolayers as novel promising 2D materials for nanoelectronics and photovoltaics. *Appl. Surf. Sci.* **2022**, *585*, 152465. [[CrossRef](#)]
- Zhang, J.; Jia, S.; Kholmanov, I.; Dong, L.; Er, D.; Chen, W.; Guo, H.; Jin, Z.; Shenoy, V.B.; Shi, L.; et al. Janus monolayer transition-metal dichalcogenides. *ACS Nano* **2017**, *11*, 8192–8198. [[CrossRef](#)]
- Taghinejad, H.; Rehn, D.A.; Muccianti, C.; Eftekhar, A.A.; Tian, M.; Fan, T.; Zhang, X.; Meng, Y.; Chen, Y.; Nguyen, T.V.; et al. Defect-mediated alloying of monolayer transition-metal dichalcogenides. *ACS Nano* **2018**, *12*, 12795–12804. [[CrossRef](#)]
- Taghinejad, H.; Eftekhar, A.A.; Adibi, A. Lateral and vertical heterostructures in two-dimensional transition-metal dichalcogenides. *Opt. Mater. Express* **2019**, *9*, 1590–1607. [[CrossRef](#)]
- Rezavand, A.; Ghobadi, N. First-principle study on quintuple-atomic-layer Janus MTeSiX_2 ($\text{M} = \text{Mo}, \text{W}; \text{X} = \text{N}, \text{P}, \text{As}$) monolayers with intrinsic Rashba spin-splitting and Mexican hat dispersion. *Mater. Sci. Semicond. Process.* **2022**, *152*, 107061. [[CrossRef](#)]
- Smidstrup, S.; Markussen, T.; Vanraeyveld, P.; Wellendorff, J.; Schneider, J.; Gunst, T.; Verstichel, B.; Stradi, D.; A Khomyakov, P.; Vej-Hansen, U.G.; et al. QuantumATK: An integrated platform of electronic and atomic-scale modelling tools. *J. Phys. Condens. Matter* **2019**, *32*, 015901. [[CrossRef](#)]
- van Setten, M.J.; Giantomassi, M.; Bousquet, E.; Verstraete, M.J.; Hamann, D.R.; Gonze, X.; Rignanese, G.-M. The PseudoDojo: Training and grading a 85 element optimized norm-conserving pseudopotential table. *Comput. Phys. Commun.* **2018**, *226*, 39–54. [[CrossRef](#)]
- Perdew, J.P.; Burke, K.; Ernzerhof, M. Generalized gradient approximation made simple. *Phys. Rev. Lett.* **1996**, *77*, 3865–3868. [[CrossRef](#)]
- Malyi, O.I.; Sopiha, K.V.; Persson, C. Energy, phonon, and dynamic stability criteria of two-dimensional materials. *ACS Appl. Mater. Interfaces* **2019**, *11*, 24876–24884. [[CrossRef](#)]
- Putungan, D.B.; Lin, S.-H.; Kuo, J.-L. A first-principles examination of conducting monolayer $1t' - \text{MX}$ ($\text{M} = \text{Mo}, \text{W}; \text{X} = \text{S}, \text{Se}, \text{Te}$): Promising catalysts for hydrogen evolution reaction and its enhancement by strain. *Phys. Chem. Chem. Phys.* **2015**, *17*, 21702–21708. [[CrossRef](#)]
- Calandra, M. Chemically exfoliated single-layer mos_2 : Stability, lattice dynamics, and catalytic adsorption from first principles. *Phys. Rev. B* **2013**, *88*, 245428. [[CrossRef](#)]

20. Heyd, J.; Peralta, J.E.; Scuseria, G.E.; Martin, R.L. Energy band gaps and lattice parameters evaluated with the Heyd–Scuseria–Ernzerhof screened hybrid functional. *J. Chem. Phys.* **2005**, *123*, 174101. [[CrossRef](#)]
21. Sibatov, R.T.; Golmankhaneh, A.K.; Meftakhutdinov, R.M.; Morozova, E.V.; Timkaeva, D.A. Modelling of electron and thermal transport in quasi-fractal carbon nitride nanoribbons. *Fractal Fract.* **2022**, *6*, 115. [[CrossRef](#)]
22. Idrees, M.; Din, H.U.; Rehman, S.U.; Shafiq, M.; Saeed, Y.; Bui, H.D.; V Nguyen, C.; Amin, B. Electronic properties and enhanced photocatalytic performance of van der Waals heterostructures of ZnO and Janus transition metal dichalcogenides. *Phys. Chem. Chem. Phys.* **2020**, *22*, 10351–10359. [[CrossRef](#)] [[PubMed](#)]
23. Idrees, M.; Din, H.U.; Ali, R.; Rehman, G.; Hussain, T.; Nguyen, C.V.; Ahmad, I.; Amin, B. Optoelectronic and solar cell applications of Janus monolayers and their van der Waals heterostructures. *Phys. Chem. Chem. Phys.* **2019**, *21*, 18612–18621. [[CrossRef](#)] [[PubMed](#)]
24. Yu, S.; Wei, W.; Li, F.; Huang, B.; Dai, Y. Electronic properties of janus MXY/graphene (M = Mo, W; X ≠ Y = S, Se) van der waals structures: A first-principles study. *Phys. Chem. Chem. Phys.* **2020**, *22*, 25675–25684. [[CrossRef](#)] [[PubMed](#)]
25. Meftakhutdinov, R.M.; Sibatov, R.T.; Kochaev, A.I.; Evseev, D.A. First-principles study of graphenylene/MoX₂ (X = S, Te, and Se) van der Waals heterostructures. *Phys. Chem. Chem. Phys.* **2021**, *23*, 14315–14324. [[CrossRef](#)]
26. Meftakhutdinov, R.M.; Kochaev, A.I.; Sibatov, R.T. Graphenylene/Janus transition metal dichalcogenides XMoY (X and Y = S, Te, Se) as a new van der Waals heterostructures for optoelectronic applications. *Phys. E Low-Dimens. Syst. Nanostruct.* **2022**, *143*, 115305. [[CrossRef](#)]
27. Cao, L.; Zhou, G.; Wang, Q.; Ang, L.K.; Ang, Y.S. Two-dimensional van der Waals electrical contact to monolayer MoSi₂N₄. *Appl. Phys. Lett.* **2021**, *118*, 013106. [[CrossRef](#)]
28. Grimme, S. Semiempirical GGA-type density functional constructed with a long-range dispersion correction. *J. Comput. Chem.* **2006**, *27*, 1787–1799. [[CrossRef](#)]